Computers and Fluids 270 (2024) 106163

Contents lists available at ScienceDirect

Computers and Fluids

journal homepage: www.elsevier.com/locate/compfluid

Artificial compressibility method for high-pressure transcritical fluids at low Mach numbers

Ahmed Abdellatif [a], Jordi Ventosa-Molina [b], Joan Grau [a], Ricardo Torres [a], Lluís Jofre [a,*]

[a] Department of Fluid Mechanics, Universitat Politècnica de Catalunya . BarcelonaTech (UPC), Barcelona 08034, Spain
[b] Department of Heat Engines, Universitat Politècnica de Catalunya . BarcelonaTech (UPC), Barcelona 08034, Spain

ARTICLE INFO

Keywords:
Artificial compressibility method
Low-Mach-number flow
Supercritical fluids
Turbulence

ABSTRACT

Supercritical fluids possess unique properties that makes them relevant in various scientific and engineering applications. However, the experimental investigation of these fluids is challenging due to the high pressures involved and their complex thermophysical behavior. To overcome these limitations, computational researchers employ scale-resolving methods, such as direct numerical simulation and large-eddy simulation to study them. Nonetheless, these methods require substantial computational resources, especially in the case of low-Mach-number regimes due to the disparity between acoustic and hydrodynamic/thermal time scales. This work, therefore, addresses this problem by extending the artificial compressibility method to high-pressure transcritical fluids. This method is based on decoupling the thermodynamic and hydrodynamic parts of the pressure field, such that the acoustic time scales can be externally modified without severely impacting the flow physics of the problem. In addition, the method proposed has two key characteristics: (i) the splitting method presents low computational complexity, and (ii) an automatic strategy for selecting the speedup factor of the approach is introduced. The effectiveness of the resulting methodology is demonstrated through comprehensive numerical tests of increasing complexity, showcasing its ability to accurately simulate a wide range of high-pressure transcritical flows including turbulence. The results obtained indicate that the approach proposed can readily lead to computational speedups larger than 10× without significantly compromising the accuracy of the numerical solutions.

1. Introduction

Supercritical fluids are substances that exist above their critical point, exhibiting distinct properties that differentiate them from both liquids and gases [1,2]. These properties include a continuous transition from liquid-like to gas-like behavior across the pseudo-boiling region. When displaying liquid-like properties, supercritical fluids are characterized by high density and transport coefficients akin to those observed in liquids. Conversely, when displaying gas-like properties, they exhibit lower density and transport coefficients resembling those observed in gases. In particular, supercritical fluids offer enhanced solubility, improved mass & heat transfer rates, and density & viscosity tunability. Consequently, these unique characteristics have captivated significant research interest across various scientific and engineering disciplines [3–6], especially in the field of energy & propulsion, like for example gas turbines, supercritical water-cooled reactors, and liquid rocket engines [7,8]. These applications demonstrate the growing prominence and relevance of high-pressure supercritical fluids in research and technological advancements. However, experimental investigations of supercritical fluids pose significant technical challenges due to the high pressures associated with them, resulting in limited quality and quantity of data obtainable through laboratory experiments or industrial procedures. To address this limitation, there is a growing interest in employing scale-resolving computational methods, such as direct numerical simulation (DNS) and large-eddy simulation (LES), to study high-pressure transcritical turbulent flows. These methods offer a notably higher level of accuracy compared to the Reynolds-averaged Navier–Stokes (RANS) approach by resolving all/most of the relevant flow scales [9,10]. As a result, the utilization of DNS/LES requires significantly greater computational resources. In this regard, large-scale parallel computations of low-Mach-number flows face difficulties in achieving efficient scalability and optimal memory utilization due to the parabolic nature of the incompressible Navier–Stokes equations. For instance, implicit time-integration schemes, although able to significantly increase time-step sizes, (i) suffer from all-to-all communication bottlenecks, (ii) require large memory resources, potentially limiting problem size and complexity, and (iii) are not efficiently suited for capturing the transient multiscale nature of turbulent flow structures.

---

* Corresponding author.
E-mail address: lluis.jofre@upc.edu (L. Jofre).

https://doi.org/10.1016/j.compfluid.2023.106163
Received 18 September 2023; Received in revised form 17 November 2023; Accepted 14 December 2023
Available online 16 December 2023
0045-7930/© 2023 The Author(s). Published by Elsevier Ltd. This is an open access article under the CC BY-NC-ND license (http://creativecommons.org/licenses/by-nc-nd/4.0/).

Conversely, compressible flow solvers exhibit more favorable characteristics for parallel calculations and memory efficiency due to their inherent explicit nature, benefiting from specialized algorithms and formulations suited for parallelization. As a result, an important body of ongoing research focuses on developing novel compressible flow solvers and adapting existing algorithms to effectively operate on modern computing architectures [11]. These architectures utilize central processing units (CPUs) equipped with accelerators, like for example graphics processing units (GPUs), which are well-suited for the task due to their ability to perform many parallel calculations simultaneously [12].

Nonetheless, the utilization of computational solvers for studying high-pressure transcritical turbulent flows presents challenges due to their inherent complex thermophysical properties. In particular, the transition from liquid-like to gas-like supercritical fluids across the pseudo-boiling line results in large variations of density and transport coefficients that require the utilization of compressible flow formulations. However, most of the scientific and engineering applications of interest related to supercritical fluids involve small flow speeds within the low-Mach-number regime. In this flow regime, a notable disparity exists between the sound speed and the fluid velocity, resulting in the fast propagation of pressure waves. This phenomenon leads to the occurrence of rapid pressure equilibration, thereby hindering the sustenance of large pressure gradients within the local fluid flow. However, it is crucial to highlight that this characteristic also renders the explicit time stepping schemes commonly employed in numerical simulations of non-stationary compressible fluid flow significantly inefficient. This inefficiency arises from the necessity of utilizing a time step size smaller than the spatial resolution multiplied by the reciprocal of the largest wave speed. Although this condition typically serves as a natural criterion for ensuring stability in transonic and supersonic flow regimes, it poses a critical limitation when dealing with low-Mach-number flows. As a result, simulating low-Mach-number flows incurs a substantial computational cost, significantly compromising the efficiency and practicality of computational simulations in this regime.

In pursuit to ameliorate this problem, the present work focuses on expanding the artificial compressibility method (ACM) to high-pressure transcritical fluids. This method artificially modifies the acoustic waves of the flow system to propagate at reduced velocities, while keeping the fluid velocity unchanged. As a result, the time step size can be significantly increased without severely impacting the flow physics of the problem. In addition, by preserving the explicit-in-time and local-in-space nature of the compressible Navier–Stokes equations, this method exhibits high parallelizability and memory efficiency. In particular, the origins of the ACM can be traced back to the seminal contributions made by Chorin [13]. Subsequent to its development, diverse adaptations of the ACM have been investigated. For instance, Philippe and Pierre [14] presented a new artificial compressibility splitting method for numerically solving unsteady incompressible viscous flows. Additionally, Asinari et al. [15] presented a novel formulation of the ACM, termed as the link-wise artificial compressibility method (LW-ACM), which exhibits comparable accuracy to traditional methods with a remarkable reduction in computational time and memory requirements. In a related development, Clausen [16] devised a numerical scheme based on the ACM for simulating incompressible flow. However, it was found that the use of artificial compressibility can lead to oscillations in the solution, particularly at high Reynolds numbers. To address this issue, Clausen introduced an entropic damping term to reduce the effect of the artificial compressibility in regions of high vorticity. This approach significantly improved the stability and accuracy of the numerical scheme, making it a valuable tool for simulating complex fluid flows. Another notable approach in this domain was presented by Guermond et al. [17]. Their method represents a generalized variant of the ACM, ensuring unconditional stability and enabling the achievement of any desired order of time accuracy. Moreover, Hejranfar et al. [18] introduced a novel preconditioning technique for incompressible flow problems with characteristic boundary conditions based on the ACM. The proposed technique involves the incorporation of a preconditioning matrix, which modifies the ACM equations and thereby mitigates the inherent stiffness of the system. The results of the study demonstrated that the preconditioned ACM offers superior computational efficiency and accuracy compared to the traditional ACM for incompressible flow problems. In addition, to broaden the applicability scope of the ACM, Dupuy et al. [19] have recently conducted a study to integrate the impacts of temperature variations and dilatation effects into the method for ideal-gas flow systems. The investigation led to the development of a highly suitable method for non-isothermal turbulent flow simulations, which can be efficiently implemented on GPU platforms due to its superior scalability. Furthermore, a recent investigation by Yasuda et al. [20] explored the impact of bulk viscosity on the stability, accuracy, and computational efficiency of the ACM for simulating unsteady incompressible fluid flow.

Expanding upon the previous discussion, this work focuses on the exploration of a solution based on the ACM in the context of high-pressure transcritical fluids at low-Mach-number flow regimes. This approach demonstrates remarkable adaptability and is particularly well-suited for performing intricate, high-fidelity simulations, while making effective use of GPU processing capabilities. In detail, the novelty of the research presented lies in the extension of the ACM to encompass real-gas behavior, in addition to the introduction of an automated strategy for selecting the optimal speedup factor for the ACM. Furthermore, the proposed method has a low-complexity structure, which enables a simple incorporation into existing computational solvers. To achieve these objectives, the paper is structured as follows. First, Section 2 provides a comprehensive description of the framework employed for the study of supercritical fluids. Following that, Section 3 presents a detailed exposition of the ACM, elucidating its principles and extension to high-pressure transcritical fluids. In Section 4, three computational experiments with different levels of physical complexity are outlined and the resulting findings are thoroughly discussed. Finally, the paper concludes by summarizing the key contributions and proposing future research directions in Section 5.

2. Flow physics modeling

The framework utilized for studying supercritical fluids turbulence in terms of (i) equations of fluid motion, (ii) real-gas thermodynamics, and (iii) high-pressure transport coefficients is described below.

2.1. Equations of fluid motion

The flow motion of supercritical fluids is described by the following set of transport equations in their compressible form, involving the conservation equations of mass, momentum, and total energy

$$\frac{\partial \rho}{\partial t} + \nabla \cdot (\rho \boldsymbol{u}) = 0, \tag{1}$$

$$\frac{\partial (\rho \boldsymbol{u})}{\partial t} + \nabla \cdot (\rho \boldsymbol{u}\boldsymbol{u}) = -\nabla P + \nabla \cdot \boldsymbol{\tau}, \tag{2}$$

$$\frac{\partial (\rho E)}{\partial t} + \nabla \cdot (\rho \boldsymbol{u} E) = -\nabla \cdot \boldsymbol{q} - \nabla \cdot (P \boldsymbol{u}) + \nabla \cdot (\boldsymbol{\tau} \cdot \boldsymbol{u}), \tag{3}$$

where ρ is the density, t is the time, $\boldsymbol{u}$ is the velocity vector, P is the pressure, $\boldsymbol{\tau} = \mu \left(\nabla \boldsymbol{u} + \nabla \boldsymbol{u}^T\right) - (2\mu/3)(\nabla \cdot \boldsymbol{u})\boldsymbol{I}$ is the viscous stress tensor with μ the dynamic viscosity and $\boldsymbol{I}$ the identity matrix, $E = e + |\boldsymbol{u}|^2/2$ and e are the total and internal energy, respectively, and $\boldsymbol{q} = -\kappa \nabla T$ is the Fourier heat conduction flux with κ the thermal conductivity and T the temperature.

2.2. Real-gas thermodynamics

The thermodynamic space of solutions for the state variables pressure P, temperature T, and density ρ of a monocomponent fluid is described by an equation of state. One popular choice for systems at high pressures, which is used in this study, is the Peng-Robinson [21] equation of state written as

$$P = \frac{R_u T}{\bar{v} - b} - \frac{a}{\bar{v}^2 + 2b\bar{v} - b^2}, \tag{4}$$

with R_u the universal gas constant, $\bar{v} = W/\rho$ the molar volume with W the molecular weight. The coefficients a and b take into account real-gas effects related to attractive forces and finite packing volume, and depend on the critical temperatures T_c, critical pressures P_c, and acentric factors ω. They are defined as

$$a = 0.457\frac{\left(\mathrm{R_u}T_c\right)^2}{P_c}\left[1 + \tilde{c}\left(1 - \sqrt{T/T_c}\right)\right]^2, \tag{5}$$

$$b = 0.078\frac{\mathrm{R_u}T_c}{P_c}, \tag{6}$$

where coefficient $\tilde{c}$ is provided as a function of acentric factor ω by

$$\tilde{c} = \begin{cases} 0.380 + 1.485\omega - 0.164\omega^2 + 0.017\omega^3 & \text{if } \omega > 0.49, \\ 0.375 + 1.542\omega - 0.270\omega^2 & \text{otherwise.} \end{cases} \tag{7}$$

The description of the thermodynamic state, i.e., enthalpy, heat capacity and entropy, needs also special consideration when dealing with supercritical fluids. This is achieved through departure functions [22], which are calculated as a difference between two states corresponding to the (i) actual supercritical condition (high pressure) and (ii) the ideal-gas condition (low pressure - only temperature dependent). The ideal-gas parts are calculated by means of the NASA 7-coefficient polynomial [23], while the analytical departure expressions to high pressures are derived from the Peng-Robinson equation of state as detailed, for example, in Jofre & Urzay [8]. In addition, the Peng-Robinson framework also provides a definition for the speed of sound [8], which for (general) real-gas thermodynamic regimes is expressed as

$$c = 1/\sqrt{\rho\beta_s}, \tag{8}$$

where $\beta_s = -(1/v)\,(\partial v/\partial P)_s$ is the isentropic compressibility and $v = 1/\rho$ is the specific volume.

2.3. High-pressure transport coefficients

The high pressures involved in the analyses conducted in this work prevent the use of simple relations for the calculation of dynamic viscosity μ and thermal conductivity κ as used for ideal gases. In this regard, standard methods for computing these coefficients for Newtonian fluids at supercritical conditions are based on the correlation expressions proposed by Chung et al. [24,25]. These correlation expressions are mainly function of critical temperature T_c and density ρ_c, molecular weight W, acentric factor ω, association factor κ_a and dipole moment $\mathcal{M}$, and the NASA 7-coefficient polynomial [23]; further details can be found in dedicated works, like for example Jofre & Urzay [8] and Poling et al. [26].

3. Artificial compressibility method

In this section, a comprehensive derivation of the artificial compressibility method for high-pressure transcritical flows developed in this study is presented. First, Section 3.1 outlines the asymptotic expansion approach utilized to decompose pressure into thermodynamic and hydrodynamic parts. Next, the modified set of transport equations in dimensionless form is described in Section 3.2. In Section 3.3, an automatic strategy for selecting the speedup factor is discussed, which is a critical aspect of this approach. Subsequently, Section 3.4 presents an analysis of the conservation properties of the ACM. Finally, the numerical methodology utilized for solving the equations of fluid motion with/out the ACM is described in Section 3.5.

3.1. Asymptotic expansion for low-mach-number flows

In the asymptotic, or perturbation, approach the stiffness of a system is mitigated through the utilization of a perturbed version of the equations. In this regard, a Taylor series expansion is utilized to express the variables in power terms of the Mach number Ma [27]. Specifically, the pressure is expanded as

$$P = P^{(0)} + \epsilon P^{(1)} + \epsilon^2 P^{(2)} + \mathcal{O}(\epsilon^3), \tag{9}$$

where $\mathbf{x}$ is the position vector, $\epsilon = \sqrt{\hat{\gamma}}Ma$ represents a small parameter proportional to Ma, $\hat{\gamma} \approx Z\gamma[(Z + T(\partial Z/\partial T)_\rho)/(Z + T(\partial Z/\partial T)_P)]$ is an approximated real-gas heat capacity ratio [28], Z is the compressibility factor, and $\gamma = c_P/c_V$ is the ideal-gas adiabatic index with c_P and c_V the specific heat capacities at constant pressure and volume, respectively. The coefficients $P^{(0)}, P^{(1)}, P^{(2)}, \ldots$ denote the zeroth, first, and second-order perturbations of pressure. It is worth noting that the expansion neglects higher-order terms, which are represented by the error term $\mathcal{O}(\epsilon^3)$.

Focusing on the limit in which Ma tends to zero, i.e., low-Mach-number regime, it is found that of the terms in Eq. (9), $P^{(0)}$ and $P^{(1)}$ have only a temporal dependency and $P^{(2)}$ a spatial and temporal dependency. Given the low Mach condition and the similar spatio-temporal dependency between $P^{(0)}$ and $P^{(1)}$, only the former is retained in the analysis. As a result, $P^{(0)}$ becomes the leading-order pressure term known as thermodynamic pressure, which is constant in space. In contrast, the second-order pressure term $P^{(2)}$ is known as hydrodynamic pressure and is responsible for ensuring that the fluid motion satisfies conservation of mass. Thus, the total pressure P can be approximated as the summation of the thermodynamic pressure $P^{(0)}(t) = P_0(t) = (1/V)\int_V P(\mathbf{x}, t)dV$, with V the volume of the domain, and the hydrodynamic pressure $P^{(2)}(\mathbf{x}, t) = \hat{\gamma}Ma^2 P_1(\mathbf{x}, t)$ in the form

$$P(\mathbf{x}, t) \approx P_0(t) + \hat{\gamma}Ma^2 P_1(\mathbf{x}, t). \tag{10}$$

3.2. Dimensionless flow equations of supercritical fluids

Following the decomposition of pressure introduced in Eq. (10), the transport equations presented in Section 2.1 can be re-expressed in dimensionless form as

$$\frac{\partial \rho^\star}{\partial t^\star} + \nabla^\star \cdot \left(\rho^\star \boldsymbol{u}^\star\right) = 0, \tag{11}$$

$$\frac{\partial\left(\rho^\star \boldsymbol{u}^\star\right)}{\partial t^\star} + \nabla^\star \cdot \left(\rho^\star \boldsymbol{u}^\star \boldsymbol{u}^\star\right) = -\nabla^\star P_1^\star + \frac{1}{Re_{\mathrm{ref}}}\nabla^\star \cdot \boldsymbol{\tau}^\star, \tag{12}$$

$$\begin{aligned}\frac{\partial\left(\rho^\star E^\star\right)}{\partial t^\star} + \nabla^\star \cdot \left(\rho^\star \boldsymbol{u}^\star E^\star\right) &= \frac{\hat{\gamma}Ma_{\mathrm{ref}}^2}{Re_{\mathrm{ref}}Pr_{\mathrm{ref}}Ec_{\mathrm{ref}}}\nabla^\star \cdot \left(\kappa^\star \nabla^\star T^\star\right) \\ &- \nabla^\star \cdot \left(P^\star \boldsymbol{u}^\star\right) + \frac{\hat{\gamma}Ma_{\mathrm{ref}}^2}{Re_{\mathrm{ref}}}\nabla^\star \cdot \left(\boldsymbol{\tau}^\star \cdot \boldsymbol{u}^\star\right),\end{aligned} \tag{13}$$

where superscript $\star$ denotes normalized quantities. The obtention of these dimensionless equations is fundamented on the following set of acoustic-based scalings [29,30]

$$\begin{aligned}&\mathbf{x}^\star = \frac{\mathbf{x}}{L_{\mathrm{ref}}}, \quad \boldsymbol{u}^\star = \frac{\boldsymbol{u}}{U_{\mathrm{ref}}}, \quad \rho^\star = \frac{\rho}{\rho_{\mathrm{ref}}}, \quad T^\star = \frac{T}{T_{\mathrm{ref}}}, \quad P^\star = \frac{P}{P_{\mathrm{ref}}}, \\ &E^\star = \frac{\rho_{\mathrm{ref}}E}{P_{\mathrm{ref}}}, \quad \mu^\star = \frac{\mu}{\mu_{\mathrm{ref}}}, \quad \kappa^\star = \frac{\kappa}{\kappa_{\mathrm{ref}}},\end{aligned} \tag{14}$$

with subscript ref indicating reference quantities, and L and U the characteristic length and velocity scales, respectively. The resulting set of scaled equations includes four dimensionless numbers: (i) Reynolds number $Re_{\mathrm{ref}} = \rho_{\mathrm{ref}}U_{\mathrm{ref}}L_{\mathrm{ref}}/\mu_{\mathrm{ref}}$ characterizing the ratio between inertial and viscous forces; (ii) Prandtl number $Pr_{\mathrm{ref}} = c_{P\mathrm{ref}}\mu_{\mathrm{ref}}/\kappa_{\mathrm{ref}}$ quantifying the ratio between momentum and thermal diffusivities; (iii) Eckert number $Ec_{\mathrm{ref}} = U_{\mathrm{ref}}^2/(c_{P\mathrm{ref}}T_{\mathrm{ref}})$ accounting for the ratio between advective mass transfer and heat dissipation potential; and (iv) Mach number $Ma_{\mathrm{ref}} = U_{\mathrm{ref}}/c_{\mathrm{ref}}$ representing the ratio of flow velocity to real-gas speed of sound approximated as $c_{\mathrm{ref}} \approx \sqrt{\hat{\gamma}R'T_{\mathrm{ref}}}$ [28], where $R' = R_u/W$ is the specific gas constant of the fluid.

3.3. Automatic selection of speedup factor

As previously introduced, the fundamental idea of ACM is to artificially reduce the acoustic time scales of the problem such that time stepping increases without severely affecting the flow physics. The first step is to express the flow variables as asymptotic expansions in the powers of the Mach number, which results in the decomposition of pressure in terms of thermodynamic and hydrodynamic parts introduced in Eq. (10). Next, the Mach number is modified to a larger value in the form $Ma' = \alpha Ma$, where $\alpha > 1$ is a speedup factor; the underlying assumption is that Ma of the initial flow is extremely small such that αMa is also sufficiently small. As a result, the total modified pressure is approximated as

$$P' \approx P_0 + \alpha^2 \hat{\gamma} Ma^2 P_1. \tag{15}$$

Consequently, the speed of sound reduces to $c' = c/\alpha$, and the acoustic time step roughly increases by a factor of order α.

The final step of the methodology is to select the value of the speedup factor α. In this regard, an automatic selection algorithm is proposed, which adjusts the value of α based on a user-specified relative error norm connected to the pressure variations of the flow that are found to exist at different times during the simulation. The objective of this algorithm is to appropriately adjust α to notably reduce the acoustic scale of the problem, while externally controlling accuracy and ensuring the stability of the solution. In particular, the user-specified relative error norm is defined as

$$\epsilon_{\mathrm{rel}} \leq \frac{|P' - P|}{|P|}, \tag{16}$$

where P denotes the original pressure, and P' is the modified pressure obtained from ACM. Introducing the definitions of P (Eq. (10)) and P' (Eq. (15)) into the expression for ϵ_{rel}, the final definition for the automated selection of α is obtained in terms of the error norms L_1, L_2, and L_∞, which will be computationally assessed in Section 4 and correspond to

$$\alpha_{L_1} \leq \sqrt{1 + \left[\frac{\epsilon_{\mathrm{rel}} \sum_i V_i |P|_i}{\sum_i V_i |\hat{\gamma} Ma^2 P_1|_i} \right]}, \tag{17}$$

$$\alpha_{L_2} \leq \sqrt{1 + \left[\frac{\epsilon_{\mathrm{rel}} \sqrt{\sum_i (V P)_i^2}}{\sqrt{\sum_i (V \hat{\gamma} Ma^2 P_1)_i^2}} \right]}, \tag{18}$$

$$\alpha_{L_\infty} \leq \sqrt{1 + \left[\frac{\epsilon_{\mathrm{rel}} P}{\hat{\gamma} Ma^2 |P_1|_\infty} \right]}, \tag{19}$$

with subindex i indicating the grid points of the computational mesh, V the corresponding grid volumes, and P approximated from Eq. (10).

3.4. Analysis of conservation properties

The ACM method proposed in this work modifies the acoustic scale of the flow by introducing a prescribed level of error in the pressure field. This error, although typically small, is in turn transferred to the conservation of momentum and total energy through the equations of fluid motion introduced above. In detail, the pressure modification impacts momentum via the pressure gradient ∇P_1, and total energy by means of the pressure power $\nabla \cdot (P\boldsymbol{u})$, where superscript $\star$ has been dropped for simplicity.

The modification of the momentum conservation properties due to the perturbation of the hydrodynamic pressure gradient ∇P_1 can be analyzed by considering the steady state inviscid limit of Eq. (12) and integrating over the entire domain. Then, introducing the definition of the error Eq. (16) into the expression of the pressure gradient results in a conservation error of momentum which scales as $[(\alpha^2 - 1)\hat{\gamma} Ma^2]$. Therefore, the error is exactly zero in the case of no acceleration, i.e., $\alpha = 1$, and for a given α value reduces exponentially (power of 2) with the Mach number of the problem.

Concerning the analysis of the conservation of total energy, the pressure power term can be split into two contributions as $\nabla \cdot (P\boldsymbol{u}) = \nabla \cdot [(P_0 + \alpha^2 \hat{\gamma} Ma^2 P_1)\boldsymbol{u}] = P_0 \nabla \cdot \boldsymbol{u} + \alpha^2 \hat{\gamma} Ma^2 \nabla \cdot (P_1 \boldsymbol{u})$. The first term $P_0 \nabla \cdot \boldsymbol{u}$ does not depend on the speedup factor α. It is in fact defined to be the same for P and P'. Consequently, this term is not affected by the ACM method. However, the second term $\alpha^2 \hat{\gamma} Ma^2 \nabla \cdot (P_1 \boldsymbol{u})$ presents the same error scaling as in the conservation of momentum.

3.5. Numerical method

The equations of fluid motion introduced above are numerically solved by adopting a standard semi-discretization procedure; viz. they are firstly discretized in space and then integrated in time. In particular, spatial operators are treated using second-order central-differencing schemes, and time-advancement is performed by means of a third-order strong-stability preserving (SSP) Runge–Kutta explicit approach [31]. The convective terms are expanded according to the Kennedy-Gruber-Pirozzoli (KGP) splitting [32,33], which has been recently extended for high-pressure supercritical fluids turbulence [34–36]. The method (i) preserves kinetic energy, (ii) is locally conservative for mass and momentum, (iii) preserves pressure equilibrium, and (iv) yields stable and robust simulations without adding any numerical diffusion to the solution or stabilization procedures.

4. Results & discussion

In this section, a series of test cases are conducted to assess the performance of the ACM proposed, which has been implemented into the in-house compressible flow solver RHEA [11]. In detail, inviscid test cases are presented in Section 4.1, followed by buoyancy-driven and turbulent flow test cases in Sections 4.2 and 4.3, respectively. The examination primarily concentrates on supercritical fluids, specifically utilizing nitrogen for the inviscid and buoyancy-driven cases, and carbon dioxide for the turbulent flow test. The critical point of nitrogen corresponds to $P_c = 3395800$ Pa and $T_c = 126.192$ K, whereas the values for carbon dioxide are $P_c = 7377270$ Pa and $T_c = 304.128$ K. The molecular weight and acentric factor for nitrogen and carbon dioxide correspond to $W = 0.02801$ kg/mol, $\omega = 0.22394$ and $W = 0.04401$ kg/mol, $\omega = 0.0372$, respectively. In addition, (i) the collapse to the incompressible limit of ACM solutions as Mach number tends to zero, and (ii) the convergence of the solution with respect to mesh resolution are analyzed in Appendix by means of a 2D Taylor–Green vortex test.

4.1. 1D two inviscid traveling waves

This test case focuses on studying the propagation of two inviscid waves in a one-dimensional (1D) system. The problem is assumed to be inviscid by setting the dynamic viscosity and thermal conductivity to zero. The domain of interest is confined to the interval $x \in [-1, 1]$ m, with a total length of $L = 2$ m. To explore a wide range of high-pressure transcritical thermodynamic conditions, the ratio of bulk (P_b) to critical (P_c) pressures P_b/P_c is set to 2.0 and 5.0, with the temperature in the domain ranging from a low ($T_l/T_c = 0.75$) to a high ($T_h/T_c = 1.5$) value. The initial conditions of the problem are as follows. The initial temperature field is given by $T(x) = T_h + [(T_h - T_l)/2][1 - \cos(2\pi x)]$, and the velocity field is uniform with initial value u_0, i.e., $u(x) = u_0$. Three specific values for the initial velocity u_0 are considered: 10, 50, and 100 m/s, corresponding to bulk Mach numbers $Ma_b \approx 0.03, 0.15, 0.3$, respectively. The characteristic time t_c is defined as $t_c = L/(2u_0)$. The time step for the simulations is determined based on the acoustic time scale, represented by $\Delta t_{\mathrm{aco}} = \mathrm{CFL}\,\Delta x / \max(|u| + c)$. In this equation, CFL refers to the Courant–Friedrichs–Lewy number, Δx represents the grid spacing, u stands for the velocity, and c denotes the speed of sound. The simulations are advanced in time until $t/t_c = 1$. To generate reference data, the problem is first simulated at very high resolution with $\Delta x/L = 1/20000$ and CFL = 0.1. Thereafter, two configurations are examined, both utilizing a coarser mesh with $\Delta x/L = 1/500$ and CFL = 0.3. One of these involves simulating the problem with the ACM turned off (ACM-off), while the other configuration considers the ACM turned on (ACM-on) with the following three values of relative error tolerance $\varepsilon_{\mathrm{rel}} = 0.01$, 0.1, 1.0.

The impact of the ACM utilization on the evolution of pressure, velocity and temperature is quantified by means of relative L_2-error norms of these magnitudes. In this regard, Table 1 presents the errors for the ACM-off configuration compared to the reference solutions for the different Mach numbers and pressure ratios considered. Notably, the errors across the variables are significantly small for all cases, especially for the $P_b/P_c = 5$ cases, indicating that the coarse grid is sufficient to resolve the present case. The differences observed in velocity, pressure and temperature with respect to the reference solutions when activating the ACM with different $\varepsilon_{\mathrm{rel}}$ values using the L_1, L_2, and L_∞-error norms are summarized in Tables 2 and 3. The results reveal that the selection of the error norm does not exert a substantial influence on the errors in the variables. Given that the determination of α primarily hinges on the pressure term, and the errors in pressure derived from various norms exhibit comparable magnitudes, it can be deduced that the choice of α remains relatively consistent across all cases, with only slight variations depending on the specific norm employed. This consistency in the selection of α yields consistent speedup outcomes. Nevertheless, it is important to acknowledge that the L_∞-norm is more responsive to substantial errors or outliers, whereas the L_1-norm exhibits greater robustness in the presence of such errors or outliers. This distinction is particularly notable when considering the highest error value of $\varepsilon_{\mathrm{rel}} = 1.0$ and the lowest Mach number $Ma_b = 0.03$. On the other hand, the L_2-norm provides an efficient balance between these two behaviors, providing a more moderate assessment of the error magnitude. In light of these observations, the subsequent analyses will primarily focus on utilizing the ACM method with the L_2-norm as a representative compromise between the L_1 and L_∞ norms.

Turning the attention now to the ACM configuration and its effects on the solved fields for the L_2-norm errors (central columns) in Table 2, the $Ma_b = 0.03$ case exhibits velocity errors of 4.12E−04 and 4.02E−04 for $\varepsilon_{\mathrm{rel}} = 0.01$ and 0.1, respectively. These errors closely align with the velocity errors reported in Table 1 for the corresponding $\varepsilon_{\mathrm{rel}}$ values, indicating a strong agreement between the ACM-on results and the reference solution. However, for the $\varepsilon_{\mathrm{rel}} = 1.0$ case, the L_2-norm velocity error significantly increases to 1.77E−03 with respect to the ACM-off case, displaying a deviation in accuracy when subjected to a higher relative error. A similar behavior is observed for the L_2-norm pressure error, indicating a larger degradation of the errors than the allowed error in $\varepsilon_{\mathrm{rel}}$. Directing the attention to the accuracy of temperature values at $Ma_b = 0.03$, the L_2-norm temperature errors for the three $\varepsilon_{\mathrm{rel}}$ values considered demonstrate remarkable consistency with the temperature errors reported in Table 1. Shifting the focus to higher Mach numbers, particularly $Ma_b = 0.3$, variations in velocity, pressure and temperature exhibit deviations of less than 0.2%, even for the highest $\varepsilon_{\mathrm{rel}}$ considered. This similarity between ACM-on and off is a result of the ACM method having a smaller effect at higher Mach numbers. In these cases, reducing the acoustic scale will reach a point where the flow speed becomes the dominating effect in the time step calculation. As a result, no speedup is achieved in these cases as discussed later in detail. Focusing on the highest pressure ratio case $P_b/P_c = 5.0$ in Table 3, it can be seen that the overall behavior is similar to the discussions above. At low-Mach-numbers with high relative errors $\varepsilon_{\mathrm{rel}}$, marked errors in the solution variables are observed. In the other cases, viz. small Mach numbers and small $\varepsilon_{\mathrm{rel}}$, the effect of the ACM on the solution variables is virtually negligible. In conclusion, the overall error magnitudes presented in Tables 2 and 3 closely resemble the values reported in Table 1, underscoring the effectiveness of the ACM method in reducing the speed of traveling waves without significantly impacting the flow physics of the problem.

The next step is to evaluate the influence of the parameter α on the computational speedup for different values of P_b/P_c and Ma_b. It is important to note that the optimal value of α varies depending on the Mach number, with higher values of α generally leading to faster computations as demonstrated in Table 4, however, at the expense of slightly less accurate results as analyzed in the paragraphs above. In particular, this table provides insights into the values of α and the corresponding speedups achieved at different Ma_b and P_b/P_c values. Upon examining the results for different P_b/P_c ratios, specifically focusing on the case of $P_b/P_c = 2$, several notable observations can be made. Firstly, increasing the value of $\varepsilon_{\mathrm{rel}}$ leads to larger values of α and, consequently, time steps. This trend is consistent across all Mach numbers. The larger α indicates a greater alteration of the simulation's speed of sound and scaling of the hydrodynamic pressure fluctuations P_1. Analyzing the specific values of α for each Mach number, it is observed that at $Ma_b = 0.03$, there is an increase in α by approximately 1.6× to 1.4× when comparing $\varepsilon_{\mathrm{rel}} = 0.01$ and $\varepsilon_{\mathrm{rel}} = 0.1$. For $Ma = 0.15$ and $Ma_b = 0.3$, the increase in α is consistently a factor of 3×. Considering the speedup, denoted as $\Delta t'/\Delta t$, it is observed that going from $\varepsilon_{\mathrm{rel}} = 0.01$ to 0.1 corresponds to a speedup increase of approximately 1.4× to 1.5×. In other words, increasing the error by 10× yields an approximate speedup of 50%. However, the increase in speedup from $\varepsilon_{\mathrm{rel}} = 0.1$ to 1 is roughly 20% only. Thus, a compromise between accuracy and computational gain may be achieved with an error of approximately $\varepsilon_{\mathrm{rel}} = 10\%$. It is worth noting that the largest speedups are observed at low-Mach-numbers. In particular, as Mach numbers increase, the benefits of capping the speed of sound diminish due to the higher flow speeds. Shifting the focus to the case of $P_b/P_c = 5$, similar trends to those obtained in the $P_b/P_c = 2$ case can be observed. However, there are some distinct characteristics. Generally, the values of α also increase by 3× for each increase of $\varepsilon_{\mathrm{rel}}$ by a factor of 10×, except for the transition from $\varepsilon = 0.1$ to 1 at $Ma_b = 0.03$. The increase in speedup from $\varepsilon_{\mathrm{rel}} = 0.01$ to 0.1 is still larger than from $\varepsilon_{\mathrm{rel}} = 0.1$ to 1, further supporting the notion that an error of approximately $\varepsilon_{\mathrm{rel}} = 10\%$ can serve as a favorable compromise. However, the speedup increase from $\varepsilon_{\mathrm{rel}} = 0.01$ to 0.1 is no longer independent of Mach number, as observed in the $P_b/P_c = 2$ case. At higher pressure and higher Mach numbers, the sensitivity to choosing $\varepsilon_{\mathrm{rel}} = 0.1$ decreases, and it may be more advantageous to select a lower value between 0.1 and 0.01 as a compromise. While further analysis is not conducted within the scope of this study, this showcases the trade-offs involved in selecting appropriate values for $\varepsilon_{\mathrm{rel}}$ in achieving the desired accuracy and computational efficiency. In conclusion, the presented table provides compelling evidence for the significant influence of the chosen α value on the computational efficiency of the numerical simulations. The results underscore the robustness and effectiveness of the ACM-on configuration across different pressure ratio scenarios, showcasing its capability to enhance computational efficiency without compromising accuracy. It is important to note that although the impact of the ACM method on the level of accuracy is not particularly pronounced in this inviscid case, its significance becomes more apparent when analyzing more complex cases in subsequent sections. This highlights the relevance of carefully selecting an appropriate value of α that strikes an optimal balance between computational speedup and numerical accuracy. Such a decision is crucial to ensure efficient and reliable simulations for a wide range of fluid flow problems.

The results presented in Table 4 are further analyzed qualitatively in Fig. 1. In particular, Fig. 1(a) depicts the normalized temperature T/T_c along x/L for $Ma_b = 0.03$ and $P_b/P_c = 2.0$ at $t/t_c = 1$ for different values of $\varepsilon_{\mathrm{rel}}$, indicating that the solutions obtained with ACM-off and ACM-on on coarser meshes exhibit a high level of agreement with the reference solutions. However, as the value of $\varepsilon_{\mathrm{rel}}$ increases up to 1.0, the ACM-on cases slightly deviate (small bumps observed) from the reference solution. Moreover, Fig. 1(b) depicts the speed of

Table 1
Numerical results for the ACM-off cases in terms of velocity (u), pressure (P) and temperature (T) relative L_2-norm errors compared to the reference solutions. The table presents results for different P_b/P_c and Ma_b values.

$P_b/P_c = 2.0$								
$Ma_b = 0.03$			$Ma_b = 0.15$			$Ma_b = 0.3$		
u_{L_2}	P_{L_2}	T_{L_2}	u_{L_2}	P_{L_2}	T_{L_2}	u_{L_2}	P_{L_2}	T_{L_2}
4.17E−04	2.84E−04	4.17E−03	3.44E−04	4.00E−04	4.17E−03	2.72E−04	6.27E−04	4.17E−03
$P_b/P_c = 5.0$								
$Ma_b = 0.03$			$Ma_b = 0.15$			$Ma_b = 0.3$		
u_{L_2}	P_{L_2}	T_{L_2}	u_{L_2}	P_{L_2}	T_{L_2}	u_{L_2}	P_{L_2}	T_{L_2}
5.98E−05	3.40E−06	7.78E−04	4.69E−05	5.30E−05	7.89E−04	7.34E−05	4.07E−05	7.84E−04

Table 2
Numerical results for the ACM-on cases in terms of velocity (u), pressure (P) and temperature (T) relative L_2-norm errors compared to reference solutions for different α values with L_1, L_2 and L_∞ norms. The table presents results for different Ma_b at $P_b/P_c = 2.0$.

$P_b/P_c = 2.0,\ Ma_b = 0.03$									
$\varepsilon_{\mathrm{rel}}$	α_{L_1}			α_{L_2}			α_{L_∞}		
	u_{L_2}	P_{L_2}	T_{L_2}	u_{L_2}	P_{L_2}	T_{L_2}	u_{L_2}	P_{L_2}	T_{L_2}
0.01	4.12E−04	2.84E−04	4.17E−03	4.12E−04	2.84E−04	4.17E−03	4.13E−04	2.84E−04	4.17E−03
0.1	4.02E−04	2.84E−04	4.17E−03	4.01E−04	2.84E−04	4.16E−03	4.00E−04	2.84E−04	4.16E−03
1.0	2.53E−03	3.45E−03	4.16E−03	1.77E−03	1.31E−03	4.17E−03	4.79E−04	3.52E−04	4.17E−03
$P_b/P_c = 2.0,\ Ma_b = 0.3$									
$\varepsilon_{\mathrm{rel}}$	α_{L_1}			α_{L_2}			α_{L_∞}		
	u_{L_2}	P_{L_2}	T_{L_2}	u_{L_2}	P_{L_2}	T_{L_2}	u_{L_2}	P_{L_2}	T_{L_2}
0.01	2.72E−04	6.25E−04	4.14E−03	2.72E−04	6.26E−04	4.16E−03	2.72E−04	6.27E−04	4.16E−03
0.1	2.72E−04	6.25E−04	4.14E−03	2.72E−04	6.27E−04	4.17E−03	2.72E−04	6.27E−04	4.17E−03
1.0	2.71E−04	6.25E−04	4.15E−03	2.71E−04	6.25E−04	4.12E−03	2.72E−04	6.25E−04	4.14E−03

Table 3
Numerical results for the ACM-on cases in terms of velocity (u), pressure (P) and temperature (T) relative L_2-norm errors compared to reference solutions for different α values with L_1, L_2 and L_∞ norms. The table presents results for different Ma_b at $P_b/P_c = 5.0$.

$P_b/P_c = 5.0,\ Ma_b = 0.03$									
$\varepsilon_{\mathrm{rel}}$	α_{L_1}			α_{L_2}			α_{L_∞}		
	u_{L_2}	P_{L_2}	T_{L_2}	u_{L_2}	P_{L_2}	T_{L_2}	u_{L_2}	P_{L_2}	T_{L_2}
0.01	5.97E−05	3.38E−06	7.87E−04	5.97E−05	3.39E−06	7.82E−04	5.98E−05	3.38E−06	7.87E−04
0.1	5.75E−05	3.25E−06	8.02E−04	5.73E−05	3.22E−06	8.34E−04	5.78E−05	3.22E−06	8.64E−04
1.0	9.27E−03	3.17E−03	8.82E−04	3.46E−03	1.28E−03	7.83E−04	6.76E−04	2.29E−04	8.59E−04
$P_b/P_c = 5.0,\ Ma_b = 0.3$									
$\varepsilon_{\mathrm{rel}}$	α_{L_1}			α_{L_2}			α_{L_∞}		
	u_{L_2}	P_{L_2}	T_{L_2}	u_{L_2}	P_{L_2}	T_{L_2}	u_{L_2}	P_{L_2}	T_{L_2}
0.01	7.34E−05	4.06E−05	8.88E−04	7.34E−05	4.06E−05	8.11E−04	7.34E−05	4.06E−05	8.24E−04
0.1	7.34E−05	4.05E−05	1.04E−03	7.34E−05	4.06E−05	8.86E−04	7.34E−05	4.06E−05	8.93E−04
1.0	7.34E−05	4.06E−05	1.21E−03	7.34E−05	4.06E−05	7.82E−04	7.34E−05	4.06E−05	7.84E−04

Table 4
Numerical results for the ACM-on cases in terms of speedup factor α and $\Delta t'/\Delta t$ ratios obtained utilizing the L_2-norm. The table presents results for different Ma_b and P_b/P_c values.

$P_b/P_c = 2.0$								
$Ma_b\ = 0.03$			$Ma_b\ = 0.15$			$Ma_b\ = 0.3$		
$\varepsilon_{\mathrm{rel}}$	α_{L_2}	$\Delta t'/\Delta t$	$\varepsilon_{\mathrm{rel}}$	α_{L_2}	$\Delta t'/\Delta t$	$\varepsilon_{\mathrm{rel}}$	α_{L_2}	$\Delta t'/\Delta t$
0.01	11.72	9.13	0.01	6.93	4.05	0.01	4.31	2.53
0.1	18.97	12.85	0.1	21.84	6.25	0.1	13.31	3.67
1.0	27.86	16.31	1.0	69.47	7.56	1.0	42.00	4.30
$P_b/P_c = 5.0$								
$Ma_b\ = 0.03$			$Ma_b\ = 0.15$			$Ma_b\ = 0.3$		
$\varepsilon_{\mathrm{rel}}$	α_{L_2}	$\Delta t'/\Delta t$	$\varepsilon_{\mathrm{rel}}$	α_{L_2}	$\Delta t'/\Delta t$	$\varepsilon_{\mathrm{rel}}$	α_{L_2}	$\Delta t'/\Delta t$
0.01	7.61	6.71	0.01	7.37	4.63	0.01	7.61	3.58
0.1	23.86	16.35	0.1	23.11	7.56	0.1	23.86	4.88
1.0	27.94	18.13	1.0	73.00	9.49	1.0	75.40	5.52

sound c normalized by the critical speed of sound c_c, which is equal to 207.206 m/s, along the domain length x/L. It is observed that the ACM-on method effectively reduces the speed of sound by factors between 10× and 100× as $\varepsilon_{\mathrm{rel}}$ increases from 0.01 to 1.0. Additionally, Fig. 2 presents ACM-off, ACM-on cases and the reference solutions at time levels $t/t_c\ = 0.25, 0.5, 0.75$, providing insight into the agreement degree and accuracy in representing the system dynamics. Notably, the ACM-on solution demonstrates a remarkable level of compliance with the reference solution, maintaining the characteristic behavior over time. These findings not only validate the robustness of the numerical method, but also emphasize the effectiveness of the ACM in enhancing computational speed without compromising the fidelity of the simulation. However, for higher values of $\varepsilon_{\mathrm{rel}}$, there is a trade-off between computational efficiency and accuracy. Therefore, it is evident that the choice of α plays a pivotal role in both the accuracy and computational cost of the numerical simulations. While the ACM method provides computational advantages, its effect on accuracy must be carefully considered, particularly for more complex cases.

4.2. 2D differentially-heated square cavity

The second case under investigation focuses on the analysis of a two-dimensional (2D) differentially-heated system utilizing the ACM.

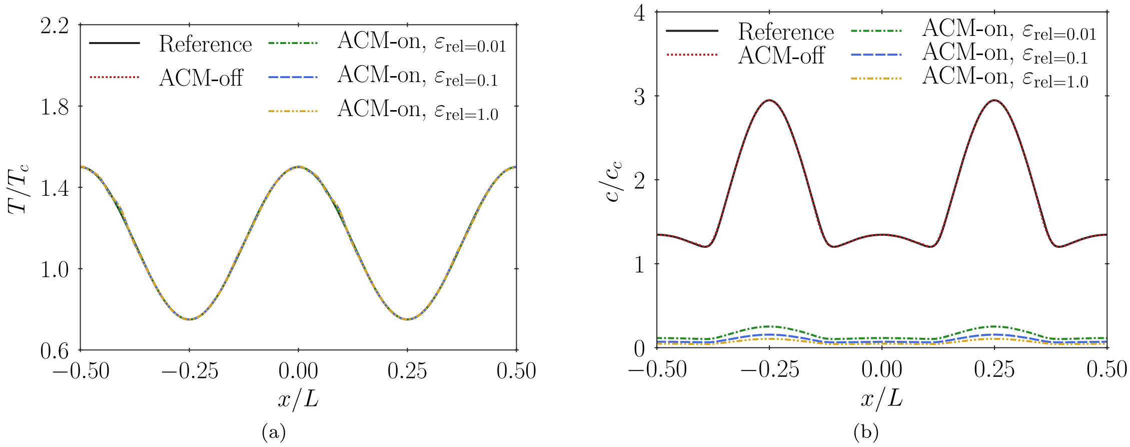

(a) (b)

Fig. 1. Temperature normalized by critical temperature T/T_c (a) and speed of sound normalized by critical speed of sound c/c_c (b) along x/L for $Ma_b = 0.03$ and $P_b/P_c = 2.0$ at $t/t_c = 1$ for different values of ε_{rel}.

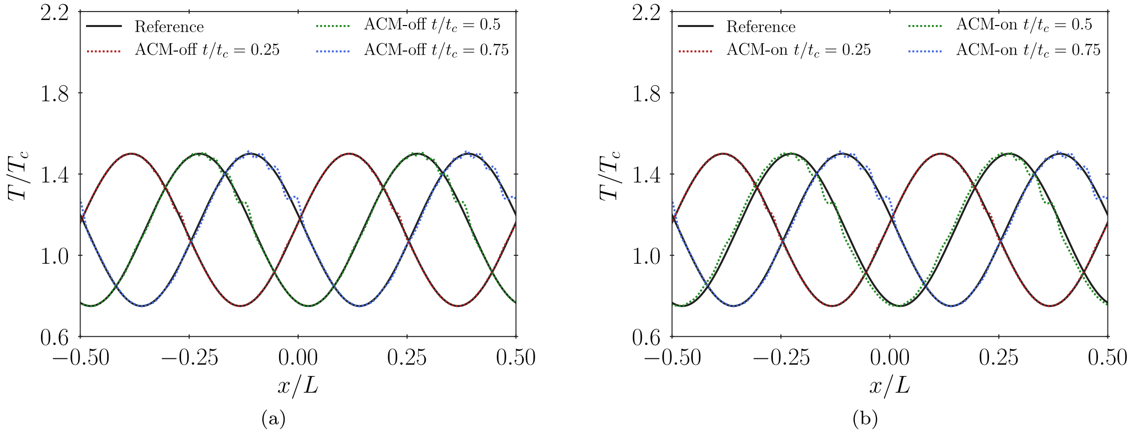

(a) (b)

Fig. 2. Temperature normalized by critical temperature T/T_c along x/L for ACM-off (a) and ACM-on with $\varepsilon_{\text{rel}} = 0.1$ (b) for $Ma_b = 0.15$ and $P_b/P_c = 2.0$ at different time levels t/t_c.

The configuration of the setup corresponds to a square cavity enclosed by hot (east) and cold (west) vertical walls and adiabatic horizontal (north & south) walls. The fluid motion is driven by natural convection resulting from a buoyancy force $-\rho g$ in the vertical direction, where $g = 9.81$ m/s^2 is the gravitational acceleration. The bulk pressure of the problem is set to $P_b/P_c = 2$, and the hot- and cold-wall temperatures are specified to $T_{hw}/T_c = 1.5$ and $T_{cw}/T_c = 0.75$, respectively. The dimensions of the cavity are set to $L = 1$ m, and the characteristic time is defined as $t_c = \sqrt{L/g} = 0.32$ s. The bulk Rayleigh number of the problem is $Ra_b = (\Delta\rho L^3\ g)/(\mu_b D_b) = 9.3\text{E}12$, with $D = \kappa/(\rho c_P)$ the thermal diffusivity, which for high-pressure transcritical fluid systems is within the laminar regime. The numerical discretization employs a mesh resolution of 192 × 192 grid points, and the simulations are advanced in time until $t/t_c = 1$ using a CFL number of 0.3. To assess the impact of errors on the accuracy of the simulations when using the ACM method, three different values of relative error tolerance $\varepsilon_{\text{rel}} = 0.01$, 0.1, 0.5 are utilized, and the automatic selection of the relaxation parameter α is determined based on the L_2-error norm.

To begin with, a general overview of the case is provided. Results of a simulation with ACM-off are presented in Fig. 3, depicting temperature, density, isobaric specific heat capacity, and speed of sound distributions within the cavity. These plots evidence the distinct gas-like and liquid-like behavior exhibited by the supercritical fluid. On the hot side, characterized by low density and dynamic viscosity, the flow presents gas-like characteristics, while close to the cold wall it presents a more liquid-like behavior. This is also evidenced by the higher speed of sound on the cold side of the cavity, reaching values 3× higher than the critical value at the bottom right corner, where temperatures are the lowest. These larger values are attributed to higher density and molecular packing levels, which result in stronger intermolecular interactions and faster propagation of pressure waves, leading to elevated values of the speed of sound, and consequently smaller values of acoustic-related time step sizes. The transition zone between phases, i.e., the pseudo-boiling region, corresponds approximately to a diagonal line, going from $(x,y)/L \approx (0.2, 0)$ to $(0.8, 1)$. In this region the isobaric specific heat capacity is largest and the density is approximately the critical one. Closing this overview, Fig. 4 shows the distribution of horizontal u and vertical v velocities in the cavity at time $t/t_c = 1$ resulting from buoyancy forces. The combined distribution of u and v indicate that the flow is following a clockwise rotational trajectory characteristic of differentially-heated cavities. Furthermore, the pseudo-boiling region presents virtually zero velocities, indicating that the phase change is affecting the flow dynamics significantly.

Before assessing the effects of the ACM, the time scales of the current case are analyzed. Fig. 5(a) and (b) present kinematic viscosity and conductivity. The former presents an inverse-like behavior compared to the isobaric specific heat capacity, in the pseudo-boiling. Additionally, it is in this region of lowest viscosity where the v-velocity becomes approximately zero. Notably, this distinctive distribution pattern is not observed for thermal conductivity, indicating a more complex relationship between fluid properties and temperature behavior in this specific scenario. This complex evolution of the flow properties have a direct impact on the flow time scales. In this regard, three main time scales are identified and discussed: (i) the acoustic time scale τ_{aco}, (ii) the viscous

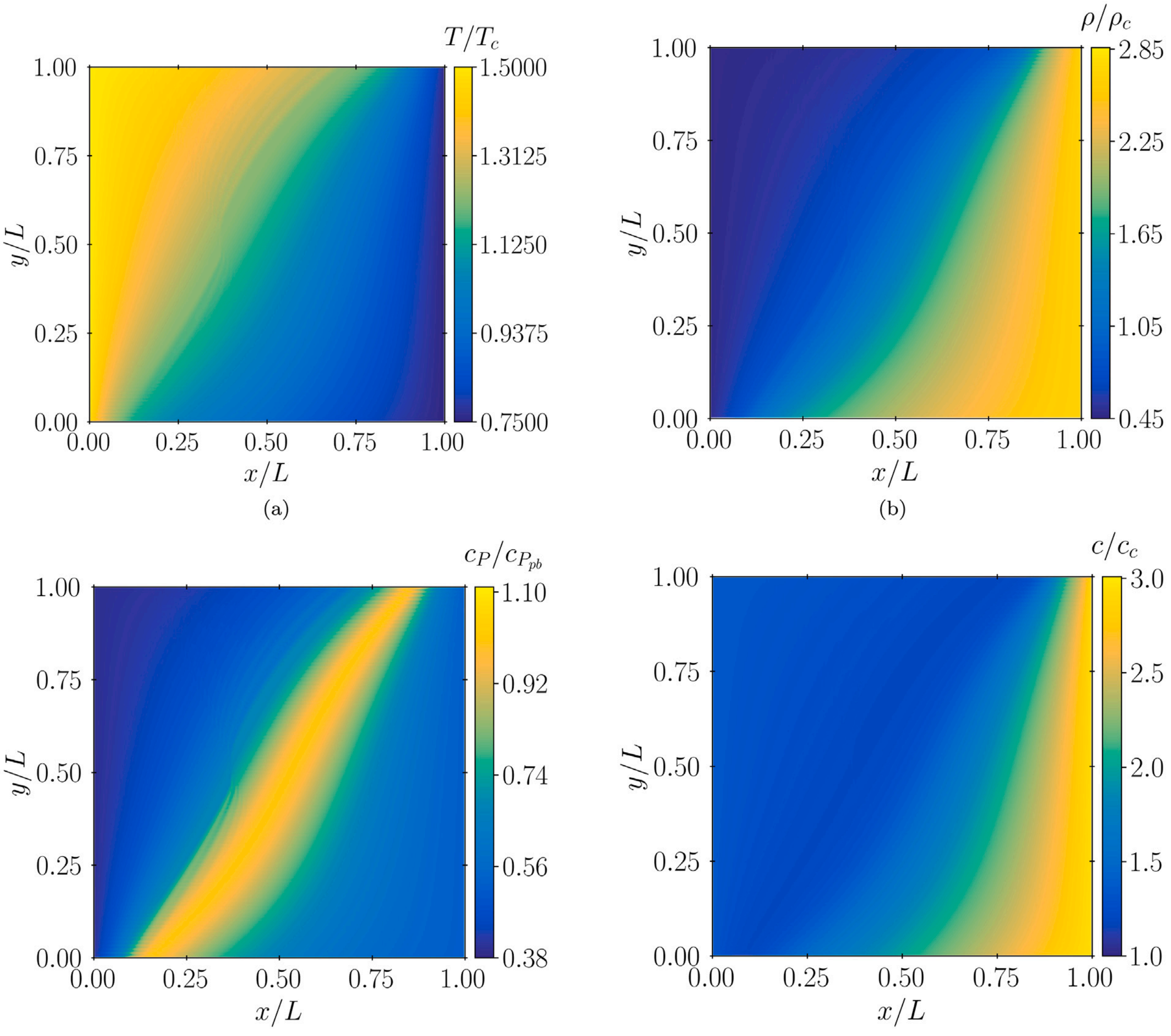

(a) (b) (c) (d)

Fig. 3. Distribution on $x/L - y/L$ of temperature normalized by critical temperature (a), density normalized by critical density (b), isobaric specific heat normalized by isobaric specific heat at pseudo-boiling point (c), and speed of sound normalized by critical speed of sound (d) obtained with ACFM-off at $t/t_c = 1$.

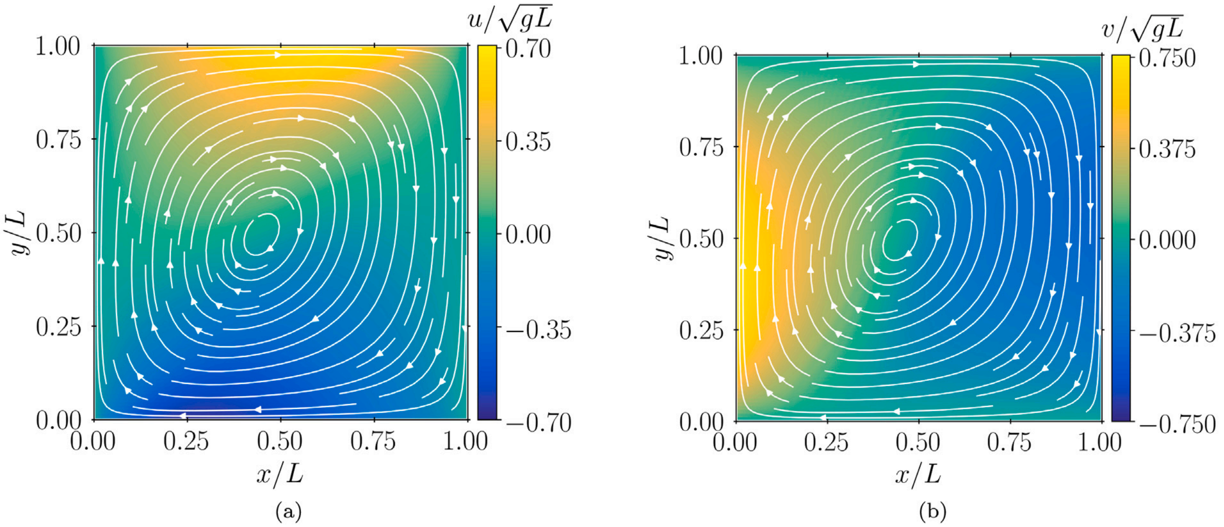

(a) (b)

Fig. 4. Distribution on $x/L - y/L$ of velocity in x (a) and y (b) directions normalized by the characteristic velocity scale obtained with ACM-off at $t/t_c = 1$; streamlines are represented by white lines.

time scale τ_{vis}, and (iii) the thermal time scale τ_{the}. The ratios between viscous and thermal time scales to the acoustic one are presented in Fig. 5(c) and (d). The viscous time scale characterizes the rate at which viscous effects propagate through the fluid domain. It is defined as the ratio of characteristic length ℓ squared to the kinematic viscosity ν as $\tau_{\text{vis}} = \ell^2/\nu$. In the context of the cavity analysis, the viscous time scale characterizes the time required for the diffusion of momentum, and is crucial in accurately capturing momentum boundary layer phenomena. The acoustic time scale, associated with the speed of sound c, on the other hand, characterizes the propagation of pressure waves through the fluid. It is defined based on the speed of sound and the characteristic length as $\tau_{\text{aco}} = \ell/c$. Lastly, the thermal time scale, represents the time required for thermal effects to propagate within the flow. In the case of the problem under consideration, the thermal time scale is critical for capturing thermal gradients, heat transfer phenomena, and accurately resolving thermal boundary layers. The thermal time scale can be determined based on the characteristic length, specific isobaric heat capacity c_P, and thermal conductivity κ as $\tau_{\text{the}} = \ell^2 c_P/\kappa$.

The computation of the time step Δt associated to each time scale is performed through the CFL criterion. For the acoustic time step, it is defined as $\Delta t_{\text{aco}} = \text{CFL}\,\Delta/\max(|u| + c)$, where $\Delta = \sqrt{\Delta x \Delta y}$ represents the grid spacing. Similarly, the time step for the viscous time scale is given by $\Delta t_{\text{vis}} = \text{CFL}\,\Delta^2/\nu$, and the time step for the thermal time scale corresponds to $\Delta t_{\text{the}} = (\text{CFL}\,\Delta^2\,c_P)/\kappa$. In connection to these definitions, Fig. 5(c) and (d) illustrate the influence of kinematic viscosity and thermal conductivity on the magnitudes of their corresponding time steps, namely the viscous and thermal time steps, in comparison to the acoustic time step. At low-pressure conditions, the kinematic viscosity of most fluids typically takes values around 10^{-5} m^2/s [37]. However, in high-pressure scenarios, such as the one considered in this case, the kinematic viscosity decreases significantly, reaching values in the order of 10^{-8} m^2/s, which is three orders of magnitude smaller. Consequently, this reduction in kinematic viscosity leads to larger time step sizes when computed based on the viscous time scale. Similarly, the thermal time step is influenced by two primary factors: (i) thermal conductivity and (ii) specific heat capacity. In the current case, due to the high-pressure conditions, the thermal conductivity is relatively high throughout the cavity. Additionally, the specific isobaric heat capacity exhibits a range of values between 1.0E03 J/(kg K) and 2.5E03 J/(kg K). Consequently, the interplay between these factors contributes to an overall increase in the magnitudes of the thermal time steps. Furthermore, considering that the speed of sound c is relatively high compared to the magnitude of the fluid velocity $|u|$, the acoustic time step size becomes very small in comparison to the viscous and thermal time steps. This discrepancy arises due to the nature of acoustic phenomena, which typically occur on much faster time scales compared to the other transport processes for low-Mach-number regimes. As a result, it can be noted that the ratios between viscous/thermal and acoustic time scales reach values in the order of 10^7, indicating that the utilization of the ACM could potentially lead to very large speedup factors by artificially reducing the speed of the acoustic waves.

As discussed in the introduction, in scenarios where the acoustic time step becomes extremely small compared to the other time steps, it can potentially constrain the time-advancement of the computations. In this regard, the results presented in Fig. 6 demonstrate the direct impact of varying ϵ_{rel} on the size of the acoustic time step. As it can be observed by the minute perturbations in the color maps, it is important to note that this significant increase in time step size comes at the expense of introducing a small error in the computation of the flow due to temporal integration inaccuracy combined with the pressure conservation error introduced by the methodology. Therefore, to evaluate the trade-off between computational time and accuracy, Table 5 details the attained speedup resulting from increasing ϵ_{rel}, as well as the observed differences in velocities and temperatures when comparing the ACM-off solutions to the cases when the ACM method is activated. Analyzing the L_2-norm errors for the velocity components u and v, it is observed that increasing ϵ_{rel} from 0.01 to 0.1 leads to an almost twentyfold increase in the error. Furthermore, a further increase of about 25% in the error is observed when transitioning from $\epsilon_{\text{rel}} = 0.1$ to 0.5. Notably, when examining the temperature field T, it is noteworthy to note that the errors for the three relative error values considered are nearly identical. This suggests that the temperature field exhibits relative insensitivity to changes in the committed relative error, essentially due to the very low-Mach-number of the present case, namely $Ma_b = 0.00024$. Focusing on the effect of the error on the changes of α and the speedup, it can be noted that the speedup gains associated to increasing ϵ_{rel} present a saturation-like behavior. Specifically, moving from $\epsilon_{\text{rel}} = 0.01$ to 0.1 results in an speedup factor increase of 1.8×, while the increase from $\epsilon_{\text{rel}} = 0.1$ to 0.5 is only 1.1×. These findings indicate that in this test case, increasing ϵ_{rel} does not result in a significant gain in terms of simulation speedup factor α.

Table 5
Relative L_2-norm errors for ACM-on of velocities $u\&v$, and temperature T, speedup factors α, and $\Delta t'/\Delta t$ ratios for Mach number $Ma_b = 0.00024$.

ϵ_{rel}	u_{L_2}	v_{L_2}	T_{L_2}	α_{L_2}	$\Delta t'/\Delta t$
0.01	7.72E−03	1.05E−02	2.21E−03	6.77	6.65
0.1	1.43E−01	1.46E−01	2.53E−03	12.57	12.11
0.5	5.48E−01	4.16E−01	7.56E−03	14.13	13.51

Overall, the results indicate that increasing the error tolerance can lead to significant speedups, with computation times up to 13.5× faster. Nonetheless, it is crucial to carefully consider the level of error acceptance based on the specific requirements of the simulation. Balancing the importance of computational time reduction with the desired level of accuracy is essential in determining an optimal value for ϵ_{rel}. Based on this analysis, the error for $\epsilon_{\text{rel}} = 10\%$ could be chosen as the upper limit of acceptable error for the present case.

4.3. 3D high-pressure transcritical turbulent channel flow

As illustrated in Fig. 7, a high-pressure transcritical turbulent channel flow at low-Mach-number conditions is selected as a final case to assess the performance of the ACM method. The fluid system is at bulk pressure of $P_b/P_c = 1.5$ and confined between isothermal walls at different temperatures, namely the cold wall (cw) and the hot wall (hw). The distance between the walls is $H = 2\delta$, where $\delta = 100\,\mu\text{m}$ represents the half-height of the channel. The temperatures at the cold and hot walls are $T_{cw}/T_c = 0.95$ and $T_{hw}/T_c = 1.1$, respectively. This setup forces the fluid to undergo a transcritical trajectory by operating within a thermodynamic region across the pseudo-boiling line [38,39]. The bulk velocity $u_b = 1$ m/s in the streamwise direction is imposed through a body force controlled by a proportional feedback loop aimed at reducing the difference between the desired and measured (numerical) values.

The computational domain is $4\pi\delta \times 2\delta \times 4/3\pi\delta$ in the streamwise (x), wall-normal (y), and spanwise (z) directions, respectively. The streamwise and spanwise boundaries are set periodic, and no-slip conditions are imposed on the horizontal boundaries (x-z planes). The grid is uniform in the streamwise and spanwise directions with resolutions in wall units (based on cw values) equal to $\Delta x^+ \approx 8.2$ and $\Delta z^+ \approx 2.7$, and stretched toward the walls in the vertical direction with the first grid point at $y^+ = y u_{\tau,cw}/\nu_{cw} \approx 0.1$ and with sizes in the range $0.18 \lesssim \Delta y^+ \lesssim 1.9$. Thus, based on preliminary studies, this grid arrangement corresponds to a DNS of size 96 × 96 × 96 grid points. For the temporal time stepping, a CFL number of 0.1 is selected. The simulation strategy starts from a linear velocity profile with random fluctuations [40], which is advanced in time to reach turbulent steady-state conditions after approximately 5 flow-through-time (FTT) units; based on the bulk velocity u_b and the length of the channel $L_x = 4\pi\delta$, a FTT is defined as $t^+ = L_x/u_b \sim \delta/u_\tau$. Flow statistics are collected for roughly 10 FTTs once steady-state conditions are achieved. For the current assessment

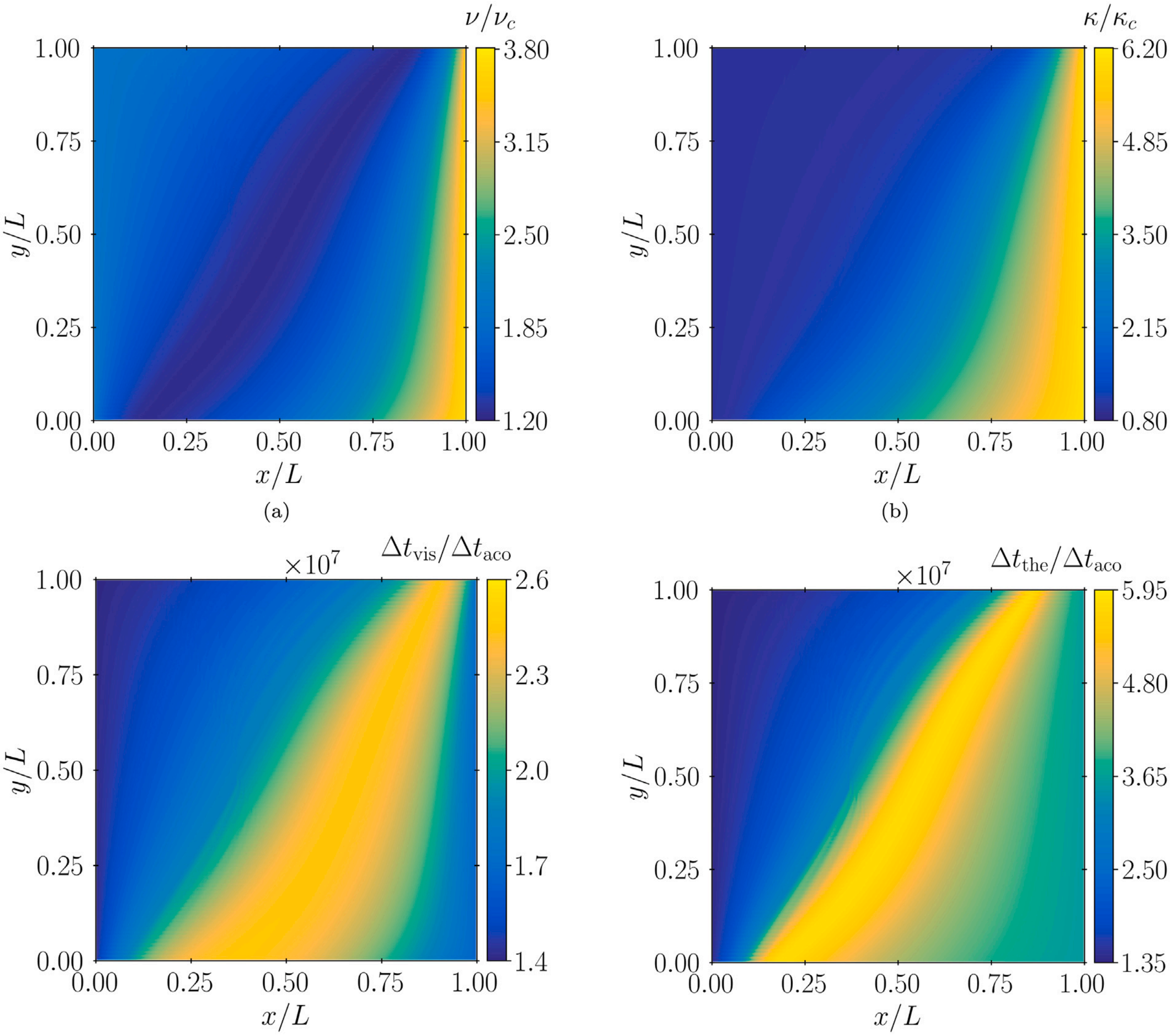

(a) (b) (c) (d)

Fig. 5. Distribution on $x/L - y/L$ of kinematic viscosity normalized by critical kinematic viscosity (a), thermal conductivity normalized by critical thermal conductivity (b), and ratios of viscous to acoustic (c) and thermal to acoustic (d) time scales obtained with ACFM-off at $t/t_c = 1$.

of the ACM method, a value of relative error tolerance ϵ_{rel} equal to 0.1 is utilized, and the automatic selection of the relaxation parameter α is determined based on the L_2-error norm.

The value of the dimensionless numbers characterizing the problem correspond to Re_b = 1942, Pr_b = 2.43, Ec_b = 7.05E−07, and Ma_b = 0.002. The time-averaged streamwise velocity u^+ and Favre-averaged root-mean-squared (rms) velocity fluctuations u^+_{rms}, v^+_{rms}, w^+_{rms} along the wall-normal direction in wall units y^+ are depicted in Fig. 8 for both ACM-off and ACM-on cases. It is important to highlight that the profiles of time-averaged streamwise velocity u^+ exhibit topological resemblances to (standard) low-pressure turbulent boundary layers. Furthermore, directing the attention to the Favre-averaged velocity fluctuations, it is noteworthy to note that turbulence intensity displays a comparable pattern between the hot/top (gas-like) and cold/bottom (liquid-like) walls along the wall-normal direction. This parity in turbulence intensity reveals itself despite the differing thermophysical properties of the fluid in the vicinity of the two walls. Focusing on temperature, different behaviors at the opposite walls can be observed. Fig. 9 depicts the mean temperature difference ΔT^+ and the Favre-averaged rms temperature fluctuations T^+_{rms}, both assessed along the wall-normal direction in wall units y^+ for the ACM-off and ACM-on cases. In detail, ΔT^+ at the cold/bottom wall increases to a maximum of approximately 10 at $y^+ \approx 100$. Additionally, the time-averaged temperature values at the cold/bottom wall are roughly 10× larger than those at the hot/top wall. This behavior is consequence of the higher thermal inertia of the supercritical liquid-like fluid found at the cold/bottom part of the channel with respect to the supercritical gas-like fluid occupying the hot/top part. This is also reflected in the temperature fluctuations, which are larger at the cold/bottom side of the channel in comparison to the hot/top region.

In terms of agreement between the results of the ACM-off and ACM-on cases, Figs. 8 and 9 indicate a virtual collapse between the curves for all the first- and second-order statistics considered. In particular, to quantify the trade-off between accuracy and computational time, Table 6 presents the speedup achieved, as well as the differences in time-averaged and fluctuating velocity and temperature values when comparing the ACM-off solutions to the case when the ACM method is activated. In the analysis of the L_2-norm errors pertaining to the velocity values, it can be observed that all errors are small in relative value. Shifting the focus to temperature, the time-averaged and

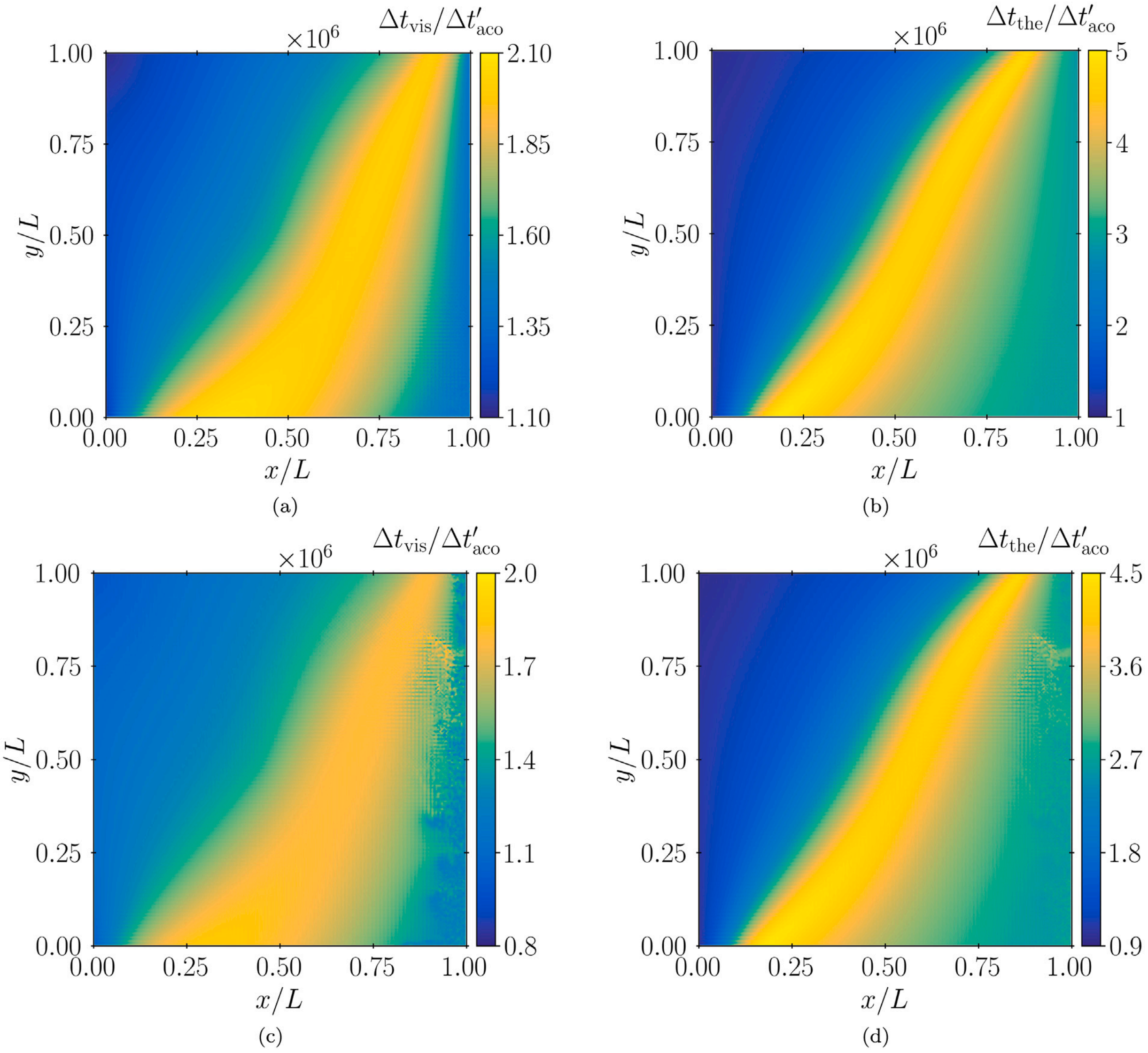

(a) (b) (c) (d)

Fig. 6. Distribution on $x/L - y/L$ of ratios between viscous to modified acoustic time scale with $\epsilon_{\mathrm{rel}} = 0.1$ (a), thermal to modified acoustic time scale with $\epsilon_{\mathrm{rel}} = 0.1$ (b), viscous to modified acoustic time scale with $\epsilon_{\mathrm{rel}} = 0.5$ (c), and thermal to modified acoustic time scale with $\epsilon_{\mathrm{rel}} = 0.5$ (d) obtained with ACM-on at $t/t_c = 1$.

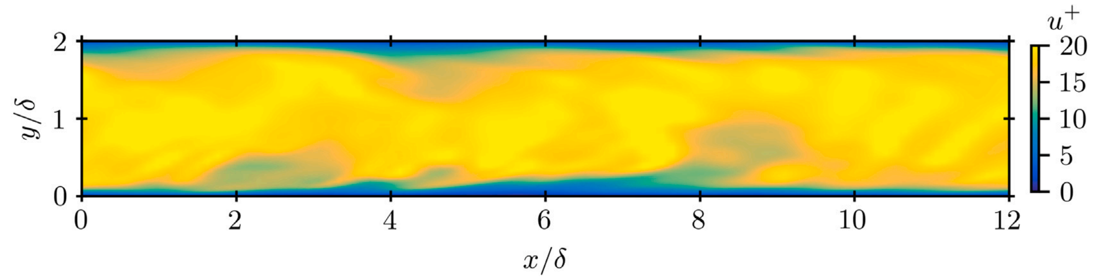

Fig. 7. Snapshot of instantaneous streamwise velocity in wall units u^+ on a x/δ-y/δ slice.

fluctuating relative errors present also significantly low values of order 10^{-4}, while achieving a computational speedup of roughly 19×. Finally, Fig. 10 serves as a further assessment of the degree of precision of the ACM-on method in representing the temporal behavior of the system. In particular, the figure depicts the time signal of instantaneous streamwise velocity u^+ and temperature T^+ at wall-normal positions $y^+ = 1$, $y^+ = 10$ and $y^+ = 100$ for the cold and hot walls in a time period ranging from $t^+ = 11$ to $t^+ = 11.1$, which corresponds to a relatively small time period solely for comparison purposes between ACM-off and ACM-on. Remarkably, the ACM-on solution exhibits a very high level

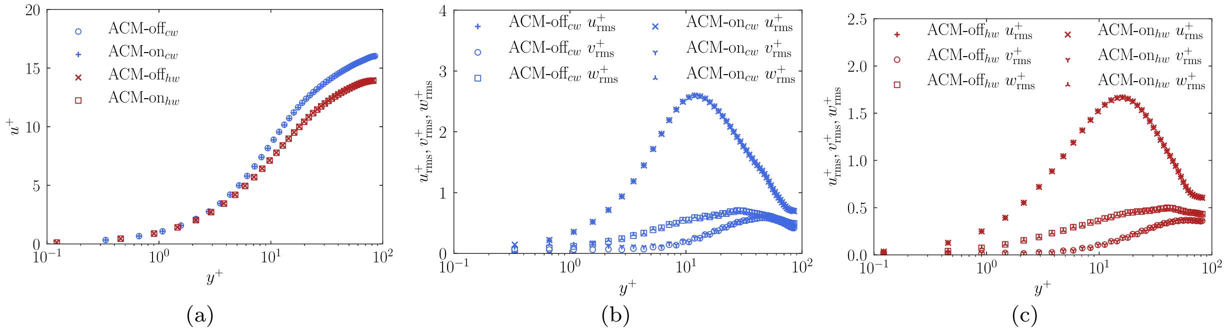

(a) (b) (c)

Fig. 8. Time-averaged mean streamwise velocity u^+ (a) and Favre-averaged rms velocity fluctuations $u^+_{\rm rms}$, $v^+_{\rm rms}$, $w^+_{\rm rms}$ at cold (b) and hot (c) walls along the wall-normal direction y^+ for the ACM-off and ACM-on cases.

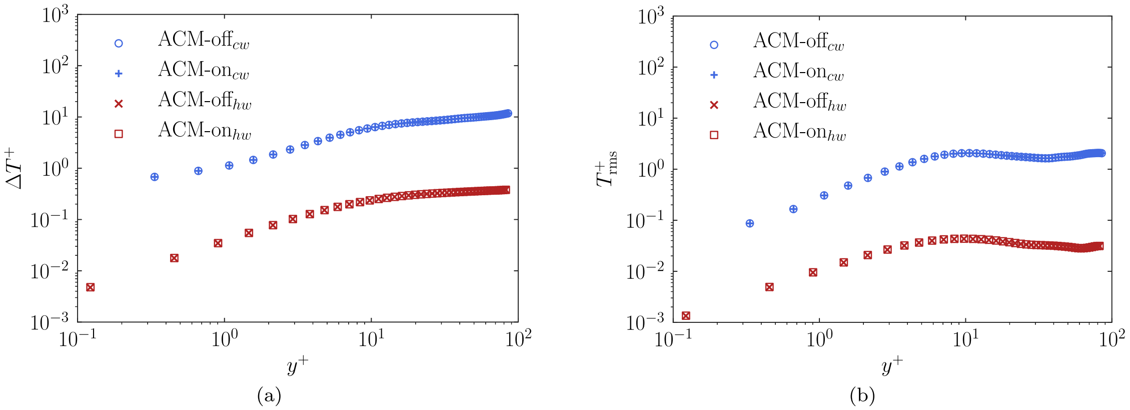

(a) (b)

Fig. 9. Mean temperature difference ΔT^+ (a) and Favre-averaged rms temperature fluctuations $T^+_{\rm rms}$ (b) along the wall-normal direction y^+ for the ACM-off and ACM-on cases at the cold and hot walls.

Table 6
Relative L_2-norm errors between ACM-off (reference) and ACM-on results of time-averaged velocity $\overline{u}$ and temperature $\overline{T}$, Favre-averaged rms fluctuations of velocity $u^+_{\rm rms}$, $v^+_{\rm rms}$, $w^+_{\rm rms}$ and temperature $T^+_{\rm rms}$, and corresponding speedup factor α and $\Delta t'/\Delta t$ ratio obtained.

$\overline{u}_{L_2}$	$\overline{T}_{L_2}$	$u^+_{\rm rms}$	$v^+_{\rm rms}$	$w^+_{\rm rms}$	$T^+_{\rm rms}$	α_{L_2}	$\Delta t'/\Delta t$
8.9E−05	1.7E−04	4.6E−04	2.0E−03	5.2E−04	5.3E−04	18.7	17.9

of congruence with the ACM-off one, preserving in this manner the flow system behavior along time. These results can be attributed to the low-Mach-number of the problem, and demonstrate that, at low fluid velocities with respect to the corresponding sound speed, the ACM method presented is able to efficiently compute complex 3D turbulent high-pressure transcritical flow problems.

5. Summary, conclusions & future work

This work has focused on extending the ACM to high-pressure transcritical flows at low Mach numbers. The study starts with introducing the equations of fluid motion modeling supercritical fluids. The subsequent section derives an ACM method specifically tailored to this investigation. This derivation incorporates two pivotal elements: (i) an elucidation of the asymptotic expansion approach, which is harnessed to decompose pressure into thermodynamic and hydrodynamic components, and (ii) the formulation of an automatic strategy for selecting the speedup factor of the ACM. To assess the effectiveness of the ACM, an array of test cases has been performed, encompassing inviscid, viscous and turbulent flow cases. These test cases serve to evaluate the numerical properties of the ACM and demonstrate its efficacy in accurately capturing the flow characteristics in diverse settings involving high-pressure transcritical flows at low Mach numbers.

The results obtained in Section 4 have demonstrated the efficacy of the ACM proposed and provided the following insight. First, as a compromise between the higher speedup and accuracy provided respectively by the L_1 and L_∞ norms, the utilization of the L_2-norm has been identified as optimal for the automatic calculation of the speedup factor α. Second, in the case of inviscid flows, computational speedups of roughly 20× can be achieved with error tolerances of 10%. Similar speedups have been obtained for significantly more complex viscous and turbulent flows with the same level of imposed error. Third, it has been identified that selecting an appropriate value of $\epsilon_{\rm rel}$ becomes essential to strike a balance between accuracy and computational efficiency. However, it is imperative to thoroughly assess the specific simulation and parallelization requirements and determine the acceptable level of accuracy and energy conservation errors to ensure the reliability of the results. In addition, it is important to highlight that this approach preserves the explicit-in-time and local-in-space nature of the compressible Navier–Stokes equations, facilitating high parallelizability and memory efficiency.

Future work will encompass further assessment of the ACM's performance for simulating high-pressure transcritical turbulent flows considering (i) different substances, (ii) wider ranges of pressure and temperature ratios, and (iii) higher Reynolds numbers. Another crucial aspect of future work involves exploring the coupling of the ACM with an implicit time integrator for the viscous terms. The present study has primarily focused on explicit-in-time integration, which offers

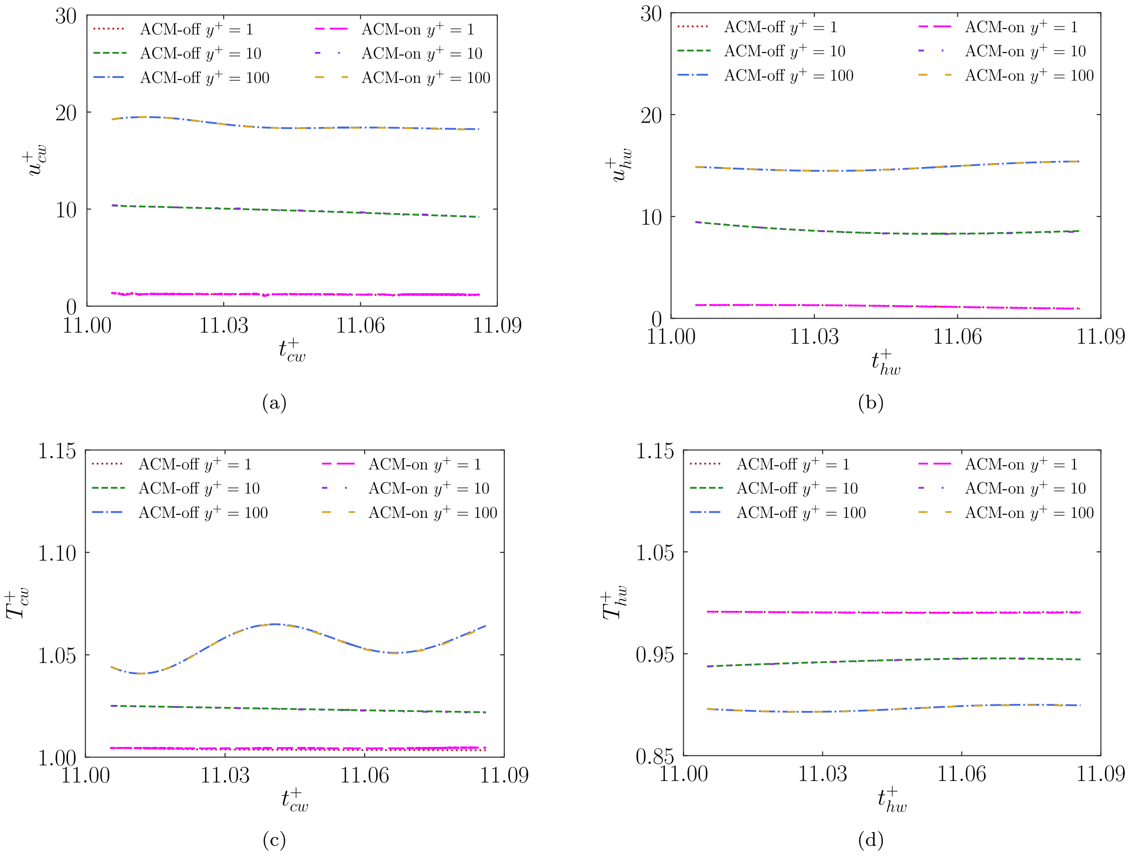

(a) (b) (c) (d)

Fig. 10. Temporal signal at wall-normal positions $y^+ = 1$, $y^+ = 10$ and $y^+ = 100$ of instantaneous streamwise velocity u^+ at cold (a) & hot (b) walls and instantaneous temperature T^+ at cold (c) & hot (d) walls for a FTT/10 starting at $t^+ = 11$ for ACM-off and ACM-on cases.

advantages in terms of parallelizability and memory efficiency. However, incorporating an implicit treatment of the viscous terms can offer numerous benefits, including larger time steps and improved numerical stability. Additionally, investigating the performance of the ACM with various high-pressure thermophysical frameworks, such as other real-gas equations of state (e.g., Virial and Wohl models) and experimental databases (e.g., REFPROP-NIST and CoolProp), and scale-resolving approaches, like for example LES, will provide valuable insights into its versatility.

CRediT authorship contribution statement

Ahmed Abdellatif: Conceptualization, Formal analysis, Investigation, Software, Writing – original draft. **Jordi Ventosa-Molina:** Conceptualization, Investigation, Writing – review & editing. **Joan Grau:** Investigation, Writing – review & editing. **Ricardo Torres:** Investigation, Writing – review & editing. **Lluís Jofre:** Conceptualization, Funding acquisition, Investigation, Writing – review & editing.

Declaration of competing interest

The authors declare that they have no known competing financial interests or personal relationships that could have appeared to influence the work reported in this paper.

Data availability

Data will be made available on request.

Acknowledgments

The authors gratefully acknowledge the SRG program (2021-SGR-01045) of the Generalitat de Catalunya (Spain), the *Beatriz Galindo* program (Distinguished Researcher, BGP18/00026) of the Ministerio de Educación y Formación Profesional (Spain), and the computer resources at FinisTerrae III & MareNostrum and the technical support provided by CESGA & Barcelona Supercomputing Center (RES-IM-2023-1-0005, RES-IM-2023-2-0005).

Funding sources

This work is funded by the European Union (ERC, SCRAMBLE, 101040379). Views and opinions expressed are however those of the authors only and do not necessarily reflect those of the European Union or the European Research Council. Neither the European Union nor the granting authority can be held responsible for them.

Appendix. 2D Taylor–Green vortex

The examination of the ACM convergence toward the incompressible limit as the Mach number reduces, and the investigation of solution convergence concerning mesh resolution, were conducted by means of the benchmark test case of the 2D Taylor–Green vortex [41]. The flow field is initialized in a square periodic domain of size $L = 2\pi$ m with an ideal gas of constant density $\rho_0 = 1$ kg/m^3, a velocity field

$$\mathbf{u} = U_0 \left[\sin x \cos y, -\cos x \sin y, 0\right]^\intercal , \tag{A.1}$$

and a pressure field

$$P = P_0 - \frac{\rho_0 U_0^2}{4} \left(\cos 2x + \cos 2y\right). \tag{A.2}$$

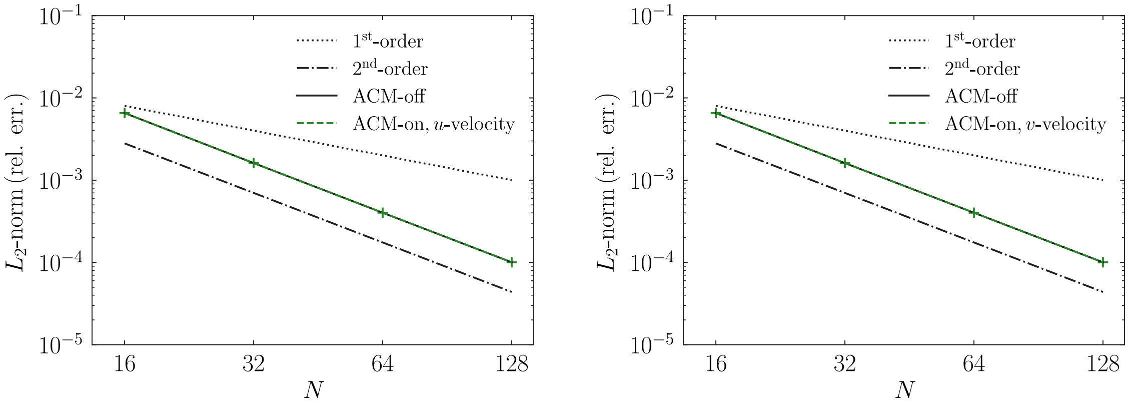

(a) (b)

Fig. A.11. Relative error convergence of the 2-D Taylor–Green vortex test in terms of u- (a) and v-velocity (b) as a function of the number of grid points $N \times N$ for the ACM-off and ACM-on cases.

Table A.7
Relative L_2-norm errors of pressure P, speedup factors α and $\Delta t'/\Delta t$ ratios for ACM-on with $\varepsilon_{\text{rel}} = 0.1$ as a function of Mach number.

Ma	P_{L_2}	α_{L_2}	$\Delta t'/\Delta t$
$10^{-1}/\sqrt{\gamma}$	3.78E−03	2.01	1.96
$10^{-2}/\sqrt{\gamma}$	3.78E−05	54.42	48.96
$10^{-3}/\sqrt{\gamma}$	3.78E−07	100.01	97.98

The reference values correspond to $U_0 = 1$ m/s, $\mu_{\text{ref}} = 1$ Pa s and $\nu_{\text{ref}} = 1$ m^2/s, aiming for specific conditions that result in Reynolds number $Re = \rho_0 U_0 \pi / \mu_{\text{ref}} = \pi$ and Mach number $Ma = U_0/\sqrt{\gamma P_0/\rho_0} = 10^{-1}/\sqrt{\gamma}$ with $\gamma = 1.4$. The equations are time-advanced to $t = \rho_0 L^2/(8\mu_{\text{ref}}\pi^2)$ units of time with a time-step corresponding to a CFL = 0.9. The analytical expressions for the velocity field are given by

$$u_{\text{exact}} = U_0 \sin(x)\cos(y)e^{-2\nu_{\text{ref}} t}, \quad v_{\text{exact}} = -U_0 \sin(x)\cos(y)e^{-2\nu_{\text{ref}} t}, \tag{A.3}$$

whereas the pressure field is described by

$$P_{\text{exact}} = P_0 - \frac{\rho_0 U_0^2}{4}\left(\cos(2x) + \cos(2y)\right) e^{-4\nu_{\text{ref}} t}. \tag{A.4}$$

The analytical solutions for u_{exact}, v_{exact}, and P_{exact} serve as benchmarks for comparison with the numerical results. The panels in Fig. A.11 show the instantaneous L2-norms of the relative errors with respect to the reference solution [41] as a function of the number of grid points $N \times N$. As expected, the rate of convergence to the analytical solution is second-order as prescribed by the spatial discretization of the solver. This observation holds true for both cases, ACM-off and ACM-on for $\varepsilon_{\text{rel}} = 0.1$. Importantly, the inclusion of ACM does not introduce any discernible impact on the convergence characteristics.

Shifting the focus to the evaluation of how the numerical solution consistently approaches the incompressible solution, Table A.7 provides detailed insights into the decreasing values of Ma down to sufficiently small Mach numbers at $\varepsilon_{\text{rel}} = 0.1$. When analyzing the L_2-norm errors for pressure P, it becomes evident that, with the reduction of Ma across the cases, specifically $Ma = 10^{-1}/\sqrt{\gamma}$, $Ma = 10^{-2}/\sqrt{\gamma}$, and $Ma = 10^{-3}/\sqrt{\gamma}$, the errors decrease by factors of 10^{-2}. This reduction aligns with the anticipated trend toward the incompressible limit, where compressibility effects become increasingly negligible. Nevertheless, a significant increase of about 100× in speedup values is observed during the transition to the lower Ma values. This observation suggests, thus, a systematic tendency of the numerical solution to asymptotically approach the incompressible solution as the Mach number monotonically reduces toward zero.

References

[1] Kiran E, Debenedetti PG, Peters CJ. Supercritical fluids: Fundamentals and applications, vol. 366. Springer Science & Business Media; 2012.
[2] Jofre L, Urzay J. A characteristic length scale for density gradients in supercritical monocomponent flows near pseudoboiling. In: Annual research briefs. Center for Turbulence Research, Stanford University; 2020, p. 277–82.
[3] Bernades M, Jofre L. Thermophysical analysis of microconfined turbulent flow regimes at supercritical fluid conditions in heat transfer applications. J Heat Transf 2022;144:082501.
[4] Clifford AA, Williams JR. Introduction to supercritical fluids and their applications. Springer; 2000.
[5] Pizzarelli M, Nasuti M, Paciorri R, Onofri M. Numerical analysis of three-dimensional flow of supercritical fluid in cooling channels. AIAA J 2009;47:2534–43.
[6] Masclans N, Vázquez-Novoa F, Bernades M, Badia RM, Jofre L. Thermodynamics-informed neural network for recovering supercritical fluid thermophysical information from turbulent velocity data. Int J Thermofluids 2023;20:100448.
[7] Yoo JY. The turbulent flows of supercritical fluids with heat transfer. Annu Rev Fluid Mech 2013;45:495–525.
[8] Jofre L, Urzay J. Transcritical diffuse-interface hydrodynamics of propellants in high-pressure combustors of chemical propulsion systems. Prog Energy Combust Sci 2021;82:100877.
[9] Jofre L, Domino SP, Iaccarino G. A framework for characterizing structural uncertainty in large-eddy simulation closures. Flow Turbul Combust 2018;100:341–63.
[10] Jofre L, Domino SP, Iaccarino G. Eigensensitivity analysis of subgrid-scale stresses in large-eddy simulation of a turbulent axisymmetric jet. Int J Heat Fluid Flow 2019;77:314–35.
[11] Jofre L, Abdellatif A, Oyarzun G. RHEA - an open-source Reproducible Hybrid-architecture flow solver Engineered for Academia. J Open Source Softw 2023;8:4637.
[12] Tölke J, Krafczyk M. TeraFlop computing on a desktop PC with GPUs for 3D CFD. Int J Comput Fluid Dyn 2008;22:443–56.
[13] Alexandre C. A numerical method for solving incompressible viscous flow problems. J Comput Phys 1997;135:118–25.
[14] Philippe A, Pierre F. Convergence results for the vector penalty-projection and two-step artificial compressibility methods. Discrete Contin Dyn Syst B 2012;17:1383–405.
[15] Asinari P, Ohwada T, Chiavazzo E, Rienzo AFD. Link-wise artificial compressibility method. J Comput Phys 2012;231:5109–43.
[16] Clausen JR. Entropically damped form of artificial compressibility for explicit simulation of incompressible flow. Phys Rev E 2013;238:175–93.
[17] Guermond J-L, Minev P. High-order time stepping for the incompressible Navier–Stokes equations. SIAM J Sci Comput 2015;37:A2656–81.
[18] Hejranfar K, Parseh K. Preconditioned c haracteristic boundary conditions based on artificial compressibility method for solution of incompressible flows. J Comput Phys 2017;346:336–54.
[19] Dupuy D, Toutant A, Bataille F. Artificial compressibility method for strongly anisothermal low Mach number flows. Phys Rev E 2021;103:013314.
[20] Yasuda T, Tanno I, Hashimoto T, Morinishi K, Satofuka N. Artificial compressibility method using bulk viscosity term for an unsteady incompressible flow simulation. Comput & Fluids 2023;105885.
[21] Peng DY, Robinson DB. A new two-constant equation of state. Ind Eng Chem Fundam 1976;15:59–64.
[22] Reynolds WC, Colonna P. Thermodynamics: Fundamentals and engineering applications. 1st ed.. Cambridge (UK): Cambridge University Press; 2019.

[23] Burcat A, Ruscic B. Third millennium ideal gas and condensed phase thermochemical database for combustion with updates from active thermochemical tables. Technical report, Argonne National Laboratory; 2005.

[24] Chung TH, Lee LL, Starling KE. Applications of kinetic gas theories and multiparameter correlation for prediction of dilute gas viscosity and thermal conductivity. Ind Eng Chem Fundam 1984;23:8–13.

[25] Chung TH, Ajlan M, Lee LL, Starling KE. Generalized multiparameter correlation for nonpolar and polar fluid transport properties. Ind Eng Chem Fundam 1988;27:671–9.

[26] Poling BE, Prausnitz JM, O'Connell JP. Properties of gases and liquids. 5th ed.. New York (USA): McGraw Hill; 2001.

[27] Dumbser C-DMM, Zucchini M. The multiple pressure variables method for fluid dynamics and aeroacoustics at low Mach numbers. Numer Methods Hyperb Kinetic Probl 2003;7:335–59.

[28] Firoozabadi A. Thermodynamics and applications in hydrocarbon energy production. 1st ed.. New York (USA): McGraw-Hill Education; 2016.

[29] Jofre L, del Rosario ZR, Iaccarino G. Data-driven dimensional analysis of heat transfer in irradiated particle-laden turbulent flow. Int J Multiph Flow 2020;125:103198.

[30] Jofre L, Bernades M, Capuano F. Dimensionality reduction of non-buoyant microconfined high-pressure transcritical fluid turbulence. Int J Heat Fluid Flow 2023;102:109169.

[31] Gottlieb S, Shu C-W, Tadmor E. Strong stability-preserving high-order time discretization methods. SIAM Rev 2001;43:89–112.

[32] Coppola G, Capuano F, Pirozzoli S, de Luca L. Numerically stable formulations of convective terms for turbulent compressible flows. J Comput Phys 2019;382:86–104.

[33] Coppola G, Capuano F, de Luca L. Discrete energy-conservation properties in the numerical simulation of the Navier-Stokes equations. Appl Mech Rev 2019;71:010803.

[34] Bernades M, Capuano F, Trias FX, Jofre L. Energy-preserving stable computations of high-pressure supercritical fluids turbulence. In: 9th European congress on computational methods in applied sciences and engineering (ECCOMAS). p. 1–12.

[35] Bernades M, Jofre L, Capuano F. Investigation of a novel numerical scheme for high-pressure supercritical fluids turbulence. In: Proceedings of the summer program 2022. Center for Turbulence Research, Stanford University; 2022, p. 225–34.

[36] Bernades M, Jofre L, Capuano F. Kinetic-energy- and pressure-equilibrium-preserving schemes for real-gas turbulence in the transcritical regime. J Comput Phys 2023;493:112477.

[37] Linstrom PJ, Mallard W. NIST chemistry webbook. 2023.

[38] Bernades M, Capuano F, Jofre L. Microconfined high-pressure transcritical fluids turbulence. Phys Fluids 2023;35:015163.

[39] Barea G, Masclans N, Jofre L. Multiscale flow topologies in microconfined high-pressure transcritical fluid turbulence. Phys Rev Fluids 2023;8:054608.

[40] Nelson KS, Fringer O. Reducing spin-up time for simulations of turbulent channel flow. Phys Fluids 2017;29:105101.

[41] Taylor GI, Green AE. Mechanism of the production of small eddies from large ones. Proc R Soc Lond Ser A 1937;158:499–521.